



# Large bandgap insulating superior clay nanosheets

Barbara Pacakova,\*<sup>1b</sup> Per Erik Vullum, Alessandro Kirch, Josef Breu, Caetano Rodrigues Miranda, and Jon Otto Fossum

One can find conductive, semiconducting, and insulating single nanosheets with unique electronic properties that are tied to their two-dimensional (2D) structure. Here, we report on wide-bandgap 2D insulator nanosheets obtained by delamination of a synthetic 2D fluorohectorite clay mineral showing one of the largest bandgap insulators in the world. The bandgap was determined experimentally to be up to 7.1–8.2 eV measured by electron energy-loss spectroscopy in a high-resolution transmission electron microscope. The experimental data were supported by DFT calculations giving a bandgap of 5.5 eV. The single fluorohectorite clay crystalline nanosheets are 0.95-nm, and they can be synthesized with high-aspect ratios and lateral dimensions up to dozens of microns. These properties render these nanosheets promising candidates for practical applications in manually assembled or self-assembled electronic heterostructures, potentially serving as insulating nanosheets in graphene or various (semi)conductive 2D material-based devices.

## Impact statement

Properties of the synthetic fluorohectorite clay presented in this article render these 0.95-nm-thin nanosheets promising candidates for practical applications in manually assembled or self-assembled electronic heterostructures, potentially serving as insulating nanosheets in graphene or various (semi)conductive 2D material-based devices.

The information provided in this work can be essential for the growing community focused on the study of 2D materials and their wide range of applications.

## Introduction

Clay minerals are among the most abundant materials in the world. The use of natural clay minerals in mostly high-tech application areas is hampered by the fact that they typically occur together with other mineral contaminants, and also exhibit inhomogeneities and defects in the structure.<sup>1–3</sup> Thus, for using these materials in high-tech applications, defect-free pure clay without contamination is needed in the first step. One very familiar example of a clay mineral-based dielectric material is mica,<sup>4,5</sup> one of the longest known dielectric materials,<sup>5</sup> which exhibits a wide bandgap of 7.85 eV. Exfoliated mica is very useful as a highly insulating nanosheet for deposition of conductive single nanosheets, such

as graphene.<sup>6–8</sup> However, delamination of mica nanosheets is not driven by thermodynamics, and can only be obtained by liquid-phase exfoliation, and thus in only small amounts when applying high-energy ultrasonication.<sup>9</sup> When reducing the number of layers in mica, the bandgap energy ( $E_g$ ) increases due to quantum size effects, as is typical for such materials, for instance hBN, dichalcogenides, black phosphorus, transition-metal oxides such as MoO<sub>2</sub>, MoO<sub>3</sub>, perovskites, topological insulators, and others.<sup>10</sup> However, despite the confirmed insulating property of bulk mica and few-layer mica,<sup>4,5,8,11</sup> there is one report suggesting that exfoliation of K-mica reduces  $E_g$  from 7.85 to 2.5 eV with reduction of the

Barbara Pacakova, Department of Physics, Norwegian University of Science and Technology-NTNU, Trondheim, Norway; barbara.pacakova@ntnu.no; barbara.pacakova@gmail.com

Per Erik Vullum, Department of Physics, Norwegian University of Science and Technology-NTNU, Trondheim, Norway; SINTEF Industry, Trondheim, Norway; PerErik.Vullum@sintef.no per.vullum@ntnu.no

Alessandro Kirch, Instituto de Física, Universidade de São Paulo-USP, Brazil; alexsandrokirch@gmail.com

Josef Breu, Bavarian Center for Battery Technology, Bavarian Polymer Institute, and Department of Chemistry, University of Bayreuth, Bayreuth, Germany; Josef.Breu@uni-bayreuth.de

Caetano Rodrigues Miranda, Instituto de Física, Universidade de São Paulo-USP, São Paulo, Brazil; crmiranda@usp.br

Jon Otto Fossum, Department of Physics, Norwegian University of Science and Technology-NTNU, Trondheim, Norway; jon.fossum@ntnu.no

\*Corresponding author

doi:10.1557/s43577-022-00349-8

number of nanosheets.<sup>12</sup> As tunneling might occur across thin nanosheets,<sup>13</sup> we propose that the reported counter intuitive result<sup>12</sup> likely could be due to the tunneling effects rather than the narrowing of the bandgap.<sup>13</sup> Apart from this one exception, all other published data show an insulating character of single mica nanosheets.<sup>5,8,11</sup> To avoid parasitic effects from impurities or defects in the experimental studies and interpretations, and further on in applications, we study here the highly crystalline and pure synthetic fluorohectorite clay (Fh), which is a close sibling of natural clay minerals and mica.<sup>14,15</sup>

The band structure of Fh nanosheets has not yet been examined. One of the most powerful techniques for  $E_g$  determination, electron energy-loss spectroscopy (EELS)<sup>16,17</sup> is utilized. The high energy resolution offered by EELS combined with the high spatial resolution of transmission electron microscopy (TEM) allows direct determination of the bandgap, without any manipulations. In EELS, fast electrons from a beam interact with the sample, causing a number of various sample excitations, including excitation of valence electrons to the conduction band. Apart from bandgap excitation, the low loss region in EELS can possibly also include bulk and surface plasmons, excitation from interband transitions or light guided modes, and Cerenkov losses.<sup>18,19</sup> However, the low refractive index (app. 1.49–1.52<sup>1,20</sup>) and limited thickness of the synthetic Fh nanosheets combined with relatively low electron-beam energies used (80-kV electrons) totally suppress Cerenkov loss and losses from guided modes. In our samples, an increase of intensity in measured spectra, for example, dependence of the intensity on energy,  $I(E)$ , thus ideally corresponds directly to the bandgap of the examined material if surface plasmons are not present.

Here, we report both a measured and DFT calculated  $E_g$  for the high-aspect ratio single Fh nanosheets proving it to be a wide-bandgap insulator.

## Results and discussion

Synthetic Fh shown in **Figure 1** is a 2:1 phyllosilicate, which typically has nominal chemical formula per half-unit-cell  $\text{Na}_{0.5} - [\text{Mg}_{(2.5)} \text{Li}_{0.5}] \text{Si}_4 \text{O}_{10} \text{F}_2$ .<sup>14,15</sup> Fh from a synthesis consists of the stacks of these 0.95-nm thin, negatively charged single nanosheets<sup>22,23</sup> kept together by charge compensating cations in the interlayer. The individual crystalline nanosheet is a “sandwich of sub-sheets” comprising three types of atomic sheets—two tetrahedral sheets of the  $\text{SiO}_2$  sandwiching one octahedral sheet, including metal elements inside (Figure 1). In Fh, the metallic sites are fully occupied by Mg and may be doped by Li, for instance.<sup>15</sup>

Fh stacks have high affinity for water intercalation in the interlayers.<sup>24,25</sup> Also, other types of molecules that are either positively charged, dipolar, or quadrupolar can be intercalated into the interlayers, depending on detailed interactions with the interlayer charges and species.<sup>26,27</sup> Examples are green house gases<sup>28–32</sup> ( $\text{CO}_2$ ,  $\text{CH}_4$ ) or pharmaceuticals.<sup>33,34</sup>

Fh crystallizes in a monoclinic crystal structure with the space group  $C2/m$  and exhibits three different hydration states

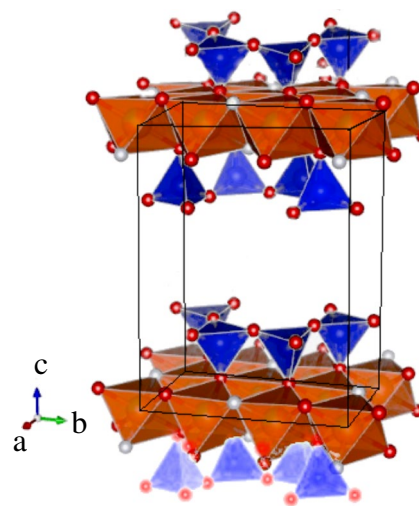


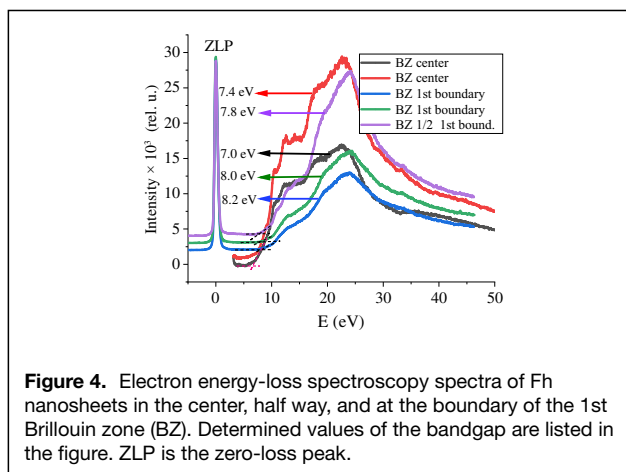
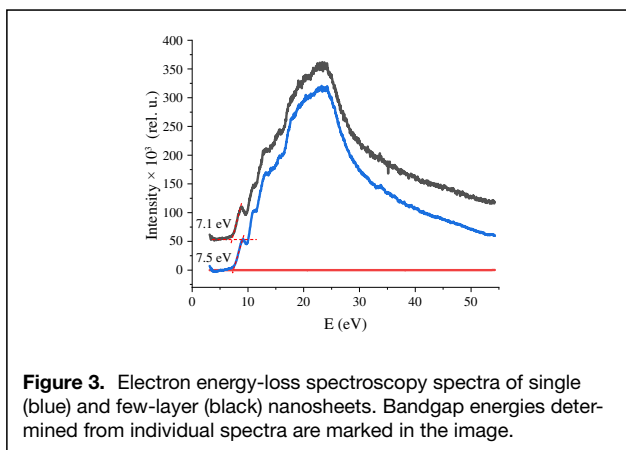
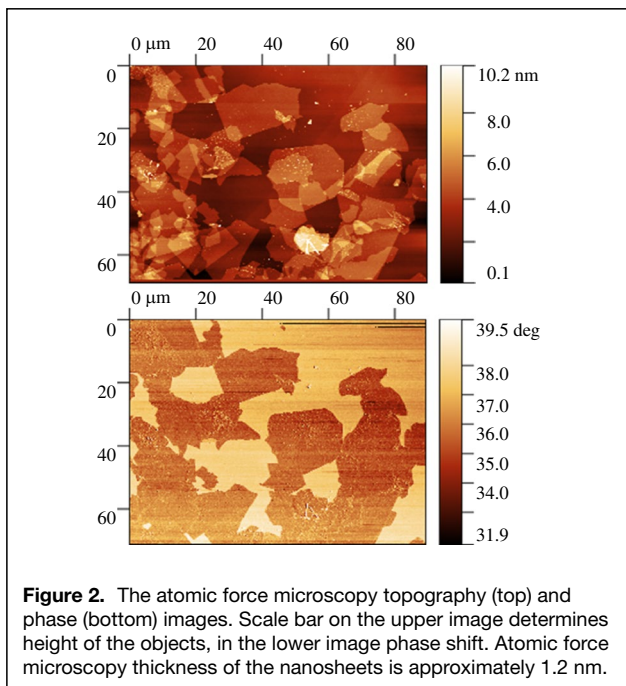
**Figure 1.** Unit-cell structure of non-hydrated Fh (without interlayer cations). In the pristine crystalline sample, nanosheets of 0.95-nm thickness are kept together by interlayer cations ( $\text{Na}^+$ ). At ambient humidity,  $\text{Na}^+$  is always hydrated.<sup>21</sup> The Fh nanosheet consists of three sheets—one octahedral (orange octahedra) and two tetrahedral (blue tetrahedra) sheets, with the octahedral sheet sandwiched between the two tetrahedral sheets. The tetrahedra consist of  $\text{SiO}_2$  and octahedra of  $\text{Mg}_{2.5} \text{Li}_{0.5} \text{O}_4 \text{F}_2$ . Lattice parameters are  $a = 5.240 \text{ \AA}$ ,  $b = 9.094 \text{ \AA}$ ,  $c = 9.40, 12.371, \text{ and } 13.60 \text{ \AA}$ , for the 0, 1, and 2 water layer hydrated clay, respectively.<sup>21</sup>

(non-hydrated, 1, and 2 water layer hydrated). Lattice parameters are  $a = 5.240 \text{ \AA}$ ,  $b = 9.094 \text{ \AA}$ , and  $c = 9.40, 12.371, \text{ and } 13.60 \text{ \AA}$  for the 0, 1, and 2 water layer hydrated clay, respectively. After immersion into liquid water, Fh exhibits complete delamination by thermodynamically driven repulsive osmotic swelling into separate single nanosheets that can form a nematic structure with parallel alignment of suspended nanosheets.<sup>14,20,23</sup>

Fh can be delaminated by thermodynamically driven repulsive osmotic swelling into high-aspect ratio single nanosheets, as shown in the AFM image (**Figure 2**). Delaminated nanosheets appear to have a thickness of about 1.2 nm. Nominal XRD thickness of single nanosheets is 0.95 nm, and the larger thickness obtained by the AFM is due to adsorbed water layer underneath the Fh single nanosheet.

TEM images showed multiple nanosheets deposited on the lacey carbon foil. Selected nanosheets were examined by EELS. Spectra from two different regions are shown in **Figure 3**. Different points of the Brillouin zone (BZ) were studied (**Figure 4**). EEL spectra from the BZ center (i.e., direct bandgap excitations are probed), half way to the 1st BZ boundary (probing indirect transitions), and at the edge of the 1st Brillouin zone were also acquired (Figure 4).

The various EELS spectra exhibit an increase of intensity at selected energies, that can be attributed to valence to conduction band excitations. The onset of the peak in the EELS spectrum corresponds to transitions from the top of the valence band to the bottom of the conduction band.<sup>35</sup> The



EELS intensity at energies above the bandgap shows however a complex profile that does not correspond to the typical parabolic shape of the free electron gas. This is attributed to contributions from plasmons and potentially other types of excitations that change the shape of intensity profile. Additionally, the captured spectra exhibit a small increase of the intensity below 7 eV. This so-called pre-absorption edge can be attributed to the formation of excitons near the minimum of the valence band, or the presence of defect states located in the bandgap.

All spectra were background subtracted by removal of the tail of the zero-loss peak (ZLP) by deconvolution of the exponential decay function in the Gatan digital micrograph software. The position of the minimum of the conduction band, which is directly attributed to  $E_g$ , was approximated by a linear fit for the signal above the peak onset,<sup>35</sup> as demonstrated in Figure 3, because the real data are far from a common theoretical model that obeying a  $I(E) \approx E^{1/2}$  dependence for the direct and a  $I(E) \approx E^3/2$  dependence for the indirect bandgap. The determined value of  $E_g$  is thus expected to slightly underestimate the real bandgap width. Moreover, direct and indirect bandgaps cannot be differentiated. All measured individual nanosheets and regions within the same nanosheet exhibit a spread of the  $E_g$  in the range of 7.1–7.5 eV, which shows that a Fh nanosheet is a wide-bandgap insulator. When scanning over the 1st Brillouin zone of Fh,  $E_g$  value ranges of 7.0–8.2 eV were found (Figure 4). This experimentally determined value of  $E_g$  is not surprising if we compare it with the  $E_g$  of individual bulk oxides forming the Fh, namely insulating MgO, and SiO<sub>2</sub>, with the *ab initio* calculated bandgaps of 3.82–7.6 for MgO,<sup>36,37</sup> and 5.67 eV<sup>35,38,39</sup> for SiO<sub>2</sub>, respectively. Experimental bandgaps of SiO<sub>2</sub> and MgO are 7.5–9.6 eV<sup>40,41</sup> and 5–7.6,<sup>37,42,43</sup> respectively. Considering these  $E_g$  values, we can conclude that a wide bandgap of Fh can arise both from the SiO<sub>2</sub> tetrahedral sheets and the metal oxides in the sandwiched octahedra.

Moreover, Fh nanosheets are prone to radiation damage by the electron beam, as can be seen in Figure 5. With increasing duration of irradiation, a gradual amorphization by beam damage was observed. Dose 7 (purple) in Figure 5 corresponds to a completely amorphized region of the sample. With increasing dose, the band  $E_g$  shifts from 7.3 eV up to 7.9 eV, approaching the value of the  $E_g$  of the SiO<sub>2</sub> and MgO.

The determined bandgap of Fh nanosheets is also close to the bulk value for mica<sup>4</sup> (7.85 eV) suggesting that it may be a good replacement for mica in applications. With readily available nanosheets, it will moreover enable faster fabrication of 2D heterostructures. Taking advantage of self-assembly properties of single Fh nanosheets, this will allow for upscaling rapid fabrication of sandwiched nanolayered structures.

To support experimental results by DFT, we estimate the Fh energy gap by calculating the band structure along the directions passing through the symmetry points of the  $Pmmm$  space group in the 1st Brillouin zone (see Figure 6). The flat

structure observed in both valence and conduction bands reveals the high effective mass and localized condition of the electrons in the system. Analysis of projected density of states

(PDOS) further reveals that the highest valence bands are mainly due to the contributions of Si and O electronic states. The highest valence and lowest conduction bands are separated by an energy bandgap of 5.55 eV at the same k-vector (direct bandgap). It is already well established that such DFT calculations underestimate the energy bandgap because it is a ground state approach.<sup>44</sup> For instance, in the case of hexagonal boron nitride (h-BN), the DFT approach returns a value in the range 4.64<sup>45,46</sup>–4.96 eV,<sup>46,46–48</sup> whereas the experimental data are in the range of 5.95<sup>49</sup>–6.8 eV<sup>50</sup> for the single h-BN sheet. Considering the differences observed in other insulators, the energy bandgap obtained for the Fh system is reasonable compared to the experimental result. Despite these differences, it is a reliable finding that the energy bandgap for the Fh is greater than the one observed in wide-gap h-BN.

We also explored the possibility of modifying the energy gap through point defects. The gradual replacement of Mg atoms by Li creates a charge imbalance in the system<sup>51</sup> and modifies the crystal symmetry. As a consequence, the energy bandgap increases as a function of the number of substitutional atoms, according to **Figure 7a**. Moreover, following standard observation of increase of the bandgap with decreasing number of nanosheets typical in 2D materials, DFT showed expected behavior also for our Fh (**Figure 7b**).

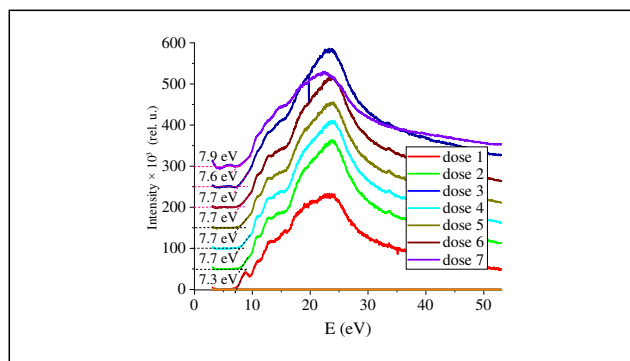


**Figure 5.** Irradiation damage by the electron beam, with dose corresponding to 15 s. With increasing dose, exposure of Fh increases by 15 s for each dose. Electron energy-loss spectroscopy spectra correspond to consecutively increasing dose, starting from nondamaged nanosheets (red spectrum, dose 1) all the way to completely amorphized nanosheets (purple spectrum, dose 7). Time scale of radiation damage is in the range of 2 minutes.

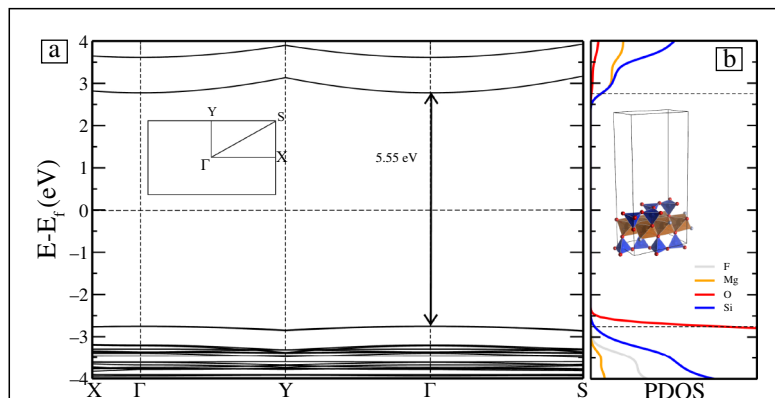


**Figure 6.** Band structure and density of states of Fh, obtained with the standard density functional theory approach. Inset panel shows the symmetry points in the 1st Brillouin zone for the *Pmm* space group. The Fermi energy ( $E_f$ ) is fixed in the middle gap. PDOS, projected density of states.

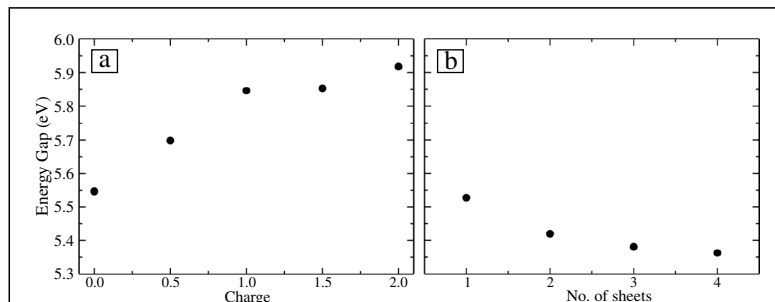


**Figure 7.** (a) Dependence of the bandgap energy for different charges of fluorohectorite nanosheets (charge per unit cell). (b) Bandgap energy dependence on the number of nanosheets.

## Methods

Synthetic Fh has been prepared as described in Reference 15. Single clay nanosheets were obtained by delamination in deionized water. The delamination was obtained by continuously shaking the 1 wt% suspension for two days. Atomic force microscope (AFM) images of the single nanosheet were obtained with a Dimension Icon (Bruker) SPM, nanoscope IV controller (Veeco–Bruker) in the tapping mode. RTESP-150 probes (with  $f_0 = 150$  kHz,  $r < 5$  nm, Bruker probes) were used, minimizing wear of the tips. To prepare samples for the AFM measurements, a very dilute ( $0.5 \times 10^{-3}$  M) nematic suspension was drop cast on clean Si and Si@SiO<sub>2</sub>(100 nm) substrates and dried overnight. Samples for EELS were prepared by drop casting the same nematic suspension on Cu TEM grids coated by “lacey carbon” films (TedPella). EELS was performed with a double Cs aberration-corrected cold FEG JEOL ARM200FC, operated at 80 kV. This instrument is equipped with a GIF Quantum ER. All EELS acquisitions were done with dual EELS and the low loss spectrum, containing the zero-loss peak (ZLP), was used to calibrate the energy scale of the bandgap spectrum. The energy resolution was measured to be 0.50 eV, based on the full width at half maximum of the ZLP. All



EELS spectra were acquired in diffraction mode with a broad beam (to avoid electron-beam damage) and where a selected-area diffraction aperture (covering a circular region of 150 nm in diameter on the sample) was used to determine what part of the sample should contribute to the EELS spectrum. All acquisitions (15 s) were taken at regions without any carbon film. All spectra were background subtracted by the removal of the tail of the zero-loss peak (ZLP) by deconvolution of the exponential decay function in the Gatan digital micrograph software. To support experimental results, we performed first-principles calculations within the DFT approach<sup>52,53</sup> to evaluate the  $E_g$  of the freestanding Fh nanosheets. To account for the dispersion of van der Waals interactions, we considered the state-of-the-art density functional developed by Berland and Hyldgaard<sup>54</sup> as implemented in the Siesta package.<sup>55</sup> The localized double-zeta polarized basis set with converged 400 Ry Mesh cutoff was adopted. The reciprocal space was represented by a grid of  $16 \times 16 \times 1$  k-points sampled with the Monkhorst–Pack scheme.

## Conclusion

For the first time, the bandgap of single fluorohectorite nanosheets has been determined, using electron energy-loss spectroscopy (EELS) and DFT calculations. The energy of the bandgap was found experimentally to be in the range of 7.1–8.2 eV, supported by DFT calculations of bandgap at 5.5 eV, which establishes that this ideal high-aspect ratio insulating single nanosheet material has one of the largest bandgap in the world. These nanosheets (0.95-nm thin, aspect ratio up to 50,000) can be used as an insulating nanosheet for deposition of graphene and various (semi)conductive 2D materials, which make them interesting candidates for fabrication of 2D-based electronic heterostructures by self-assembly or manually. The information provided in this work can be essential for the growing community focused on the study of 2D materials and their wide range of applications.

## Acknowledgments

B.P. and J.O.F. gratefully acknowledge the funding by the Research Council of Norway Nano2021, Project No. 250619. J.B. acknowledges Deutsche Forschungsgemeinschaft (SFB 840, TP A6). A.K. and C.R.M. gratefully acknowledge the Research Centre for Gas Innovation (RCGI), support from the Brazilian agencies FAPESP (2017/02317-2) and CNPq, and the resources supplied by the Centre for Scientific Computing (NCC/GridUNESP) of the São Paulo State University (UNESP).

## Author contributions

J.B. provided the fluorohectorite clay, B.P. prepared exfoliated and deposited clay nanosheets. P.E.V. and B.P. measured EELS. A.K. performed DFT calculations. B.P., P.E.V., and A.K. co-wrote the first versions of the manuscript. All authors

took part in discussions that led to the final version of the manuscript. B.P. completed the final manuscript with the aid of J.B., C.M., and J.O.F.

## Funding

Open access funding provided by NTNU Norwegian University of Science and Technology (incl St. Olavs Hospital - Trondheim University Hospital). Research Council of Norway Nano2021, Project No. 250619; Deutsche Forschungsgemeinschaft (SFB 840, TP A6); Research Centre for Gas Innovation (RCGI), FAPESP (2017/02317-2) and Centre for Scientific Computing (NCC/GridUNESP) of the São Paulo State University (UNESP).

## Data availability

Not applicable

## Code availability

Not applicable

## Conflict of interest

On behalf of all authors, the corresponding author states that there is no conflict of interest.

## Ethical approval

Not applicable

## Consent to participate

Not applicable

## Consent for publication

Not applicable

## Supplementary information

The online version contains supplementary material available at <https://doi.org/10.1557/s43577-022-00349-8>.

## Open access

This article is licensed under a Creative Commons Attribution 4.0 International License, which permits use, sharing, adaptation, distribution and reproduction in any medium or format, as long as you give appropriate credit to the original author(s) and the source, provide a link to the Creative Commons license, and indicate if changes were made. The images or other third party material in this article are included in the article's Creative Commons license, unless indicated otherwise in a credit line to the material. If material is not included in the article's Creative Commons license and your intended use is not permitted by statutory regulation or exceeds the permitted use, you will need to obtain permission directly from the copyright holder. To view a copy of this license, visit <http://creativecommons.org/licenses/by/4.0/>.



## References

1. S. Mukherjee, *Classification and Composition of Clay Constituents* (Springer, Dordrecht, 2013), pp. 23–32
2. M. Valášková, G. Simha-Martynková, "Vermiculite: Structural Properties and Examples of the Use," in *Clay Minerals in Nature - Their Characterization, Modification and Application*, M. Valaskova, Ed. (Intech Open, Vienna, 2012), pp. 209–238
3. R. Neumann, G.E.L. Costa, J.C. Gaspar, M. Palmieri, S.E.E. Silva, *Miner. Eng.* **24**, 1323 (2011). <https://doi.org/10.1016/j.mineng.2011.05.017>
4. A.T. Davison, A.F. Vickers, *J. Phys. C Solid State Phys.* **5**, 879 (1972). <https://doi.org/10.1088/0022-3719/5/8/014>
5. U. Buechner, *J. Phys. C Solid State Phys.* **8**, 2781 (1975). <https://doi.org/10.1088/0022-3719/8/17/018>
6. O. Ochedowski, B.K. Bussmann, M. Schleberger, *Sci. Rep.* **4**, 6003 (2014). <https://doi.org/10.1038/srep06003>
7. A.N. Rudenko, F.J. Keil, M.I. Katsnelson, A.I. Lichtenstein, *Phys. Rev. B* **83**(4), 045409 (2011). <https://doi.org/10.1103/PhysRevB.83.045409>
8. A. Castellanos-Gomez, M. Wojtaszek, N. Tombros, N. Agrait, B.J. Van Wees, G. Rubio-Bollinger, *Small* **7**, 2491 (2011). <https://doi.org/10.1002/sml.201100733>
9. L. Mogg, G.P. Hao, S. Zhang, C. Bacaksiz, Y.C. Zou, S.J. Haigh, F.M. Peeters, A.K. Geim, M. Lozada-Hidalgo, *Nat. Nanotechnol.* **14**, 962 (2019). <https://doi.org/10.1038/s41565-019-0536-5>
10. A. Chaves, J.G. Azadani, H. Alsalman, D.R. da Costa, R. Frisenda, A.J. Chaves, S.H. Song, Y.D. Kim, D. He, J. Zhou, A. Castellanos-Gomez, F.M. Peeters, Z. Liu, C.L. Hinkle, S.-H. Oh, P.D. Ye, S.J. Koester, Y.H. Lee, P. Avouris, X. Wang, T. Low, *NPJ 2D Mater. Appl.* **4**, 29 (2020). <https://doi.org/10.1038/s41699-020-00162-4>
11. A.J. Atkins, D.L. Misell, *J. Phys. C Solid State Phys.* **5**, 3153 (1972). <https://doi.org/10.1088/0022-3719/5/22/004>
12. S.S. Kim, T.V. Khai, V. Kulish, Y.H. Kim, H.G. Na, A. Katoch, M. Osada, P. Wu, H.W. Kim, *Chem. Mater.* **27**, 4222 (2015). <https://doi.org/10.1021/cm504802j>
13. M.R. Islam, M. Tomitori, *Appl. Surf. Sci.* **532**, 147388 (2020). <https://doi.org/10.1016/j.apsusc.2020.147388>
14. M. Stöter, S. Rosenfeldt, J. Breu, *Annu. Rev. Mater. Res.* **45**, 129 (2015). <https://doi.org/10.1146/annurev-matsci-070214-020830>
15. J. Breu, W. Seidl, A.J. Stoll, K.G. Lange, T.U. Probst, *Chem. Mater.* **13**, 4213 (2001). <https://doi.org/10.1021/cm011014m>
16. V.J. Keast, A.J. Scott, R. Brydson, D.B. Williams, J. Bruley, *J. Microsc.* **203**, 135 (2001). <https://doi.org/10.1046/j.1365-2818.2001.00898.x>
17. F.J. García de Abajo, *Rev. Mod. Phys.* **82**(1), 209 (2010). <https://doi.org/10.1103/RevModPhys.82.209>
18. M. Horák, M. Stöger-Pollach, *Ultramicroscopy* **157**, 73 (2015). <https://doi.org/10.1016/j.ultramic.2015.06.005>
19. K.A. Mkhoyan, T. Babinec, S.E. Maccagnano, E.J. Kirkland, J. Silcox, *Ultramicroscopy* **107**, 345 (2007). <https://doi.org/10.1016/j.ultramic.2006.09.003>
20. P.H. Michels-Brito, V. Dudko, D. Wagner, P. Markus, G. Papastavrou, L. Michels, J. Breu, J.O. Fossum, *Sci. Adv.* **8**, 8147 (2022). <https://doi.org/10.1126/sciadv.abl8147>
21. H. Kalo, M.W. Möller, D.A. Kunz, J. Breu, *Nanoscale* **4**, 5633 (2012). <https://doi.org/10.1039/c2nr31322g>
22. M. Stöter, S. Godrich, P. Feicht, S. Rosenfeldt, H. Thurn, J.W. Neubauer, M. Seuss, P. Lindner, H. Kalo, M. Moller, A. Fery, S. Forster, G. Papastavrou, J. Breu, *Angew. Chem. Int. Ed.* **55**, 7398 (2016). <https://doi.org/10.1002/anie.201601611>
23. S. Rosenfeldt, M. Stöter, M. Schlenk, T. Martin, R.Q. Albuquerque, S. Forster, J. Breu, *Langmuir* **32**, 10582 (2016). <https://doi.org/10.1021/acs.langmuir.6b02206>
24. U.V. Reddy, G.M. Bowers, N. Loganathan, M. Bowden, A.O. Yazaydin, R.J. Kirkpatrick, *J. Phys. Chem. C* **120**, 8863 (2016). <https://doi.org/10.1021/acs.jpcc.6b03431>
25. H. Kalo, W. Milius, J. Breu, *RSC Adv.* **2**, 8452 (2012). <https://doi.org/10.1039/c2ra20457f>
26. P. Loch, K.W.B. Hunvik, F. Puchtl, S. Weiß, K.K. Seljelid, P.M. Røren, S. Rudic, S. Raaen, K.D. Knudsen, H.N. Bordallo, J.O. Fossum, J. Breu, *Appl. Clay Sci.* **198**, 105831 (2020). <https://doi.org/10.1016/j.clay.2020.105831>
27. J.O. Fossum, *Eur. Phys. J. Spec. Top.* **229**, 2863 (2020). <https://doi.org/10.1140/epjst/e2020-000131-1>
28. L.P. Cavalcanti, G.N. Kalantzopoulos, J. Eckert, K.D. Knudsen, J.O. Fossum, *Sci. Rep.* **8**, 11827 (2018). <https://doi.org/10.1038/s41598-018-30283-2>
29. H. Hemmen, E.G. Rolseth, D.M. Fonseca, E.L. Hansen, J.O. Fossum, T.S. Plivelic, *Langmuir* **28**, 1678 (2012). <https://doi.org/10.1021/la204164q>
30. L. Michels, J.O. Fossum, Z. Rozynek, H. Hemmen, K. Rustenberg, P.A. Sobas, G.N. Kalantzopoulos, K.D. Knudsen, M. Janek, T.S. Plivelic, G.J. da Silva, *Sci. Rep.* **5**, 8775 (2015). <https://doi.org/10.1038/srep08775>
31. K.W.B. Hunvik, P. Loch, L.P. Cavalcanti, K.K. Seljelid, P.M. Røren, S. Rudic, D. Wallacher, A. Kirch, K.D. Knudsen, C. Rodrigues Miranda, J. Breu, H.N. Bordallo, J.O. Fossum, *J. Phys. Chem. C* **124**, 26222 (2020). <https://doi.org/10.1021/acs.jpcc.0c07206>
32. K.W. Bø Hunvik, P. Loch, D. Wallacher, A. Kirch, L.P. Cavalcanti, M. Rieß, M. Daab, V. Josvanger, S. Grätz, F. Yokaichiya, K.D. Knudsen, C. Rodrigues Miranda, J. Breu, J.O. Fossum, *Langmuir* **37**, 14491 (2021). <https://doi.org/10.1021/acs.langmuir.1c02467>
33. E.C. Santos, Z. Rozynek, E.L. Hansen, R.N. Klitgaard, L. Michels, A. Mikkelsen, T.S. Plivelic, H.N. Bordallo, J.O. Fossum, *RSC Adv.* **7**, 26537 (2017). <https://doi.org/10.1039/c7ra01384a>
34. E.C. Santos, W.P. Gates, L. Michels, F. Juranyi, A. Mikkelsen, G.J. Silva, J.O. Fossum, H.N. Bordallo, *Appl. Clay Sci.* **166**, 288 (2018). <https://doi.org/10.1016/j.clay.2018.09.029>
35. J. Park, S. Heo, J.G. Chung, H. Kim, H.I. Lee, K. Kim, G.S. Park, *Ultramicroscopy* **109**, 1183 (2009). <https://doi.org/10.1016/j.ultramic.2009.04.005>
36. A. Kjekshus, T. Rakke, *Acta Chem. Scand.* **A33**, 617 (1979)
37. A.M. El-Sayed, M.B. Watkins, T. Grasser, A.L. Shluger, *Phys. Rev. B* **98**, 064102 (2018). <https://doi.org/10.1103/PhysRevB.98.064102>
38. J. Chelikowsky, N. Binggeli, N. Keskar, *J. Alloys Compd.* **197**, 137 (1993). [https://doi.org/10.1016/0925-8388\(93\)90036-M](https://doi.org/10.1016/0925-8388(93)90036-M)
39. Y.-N. Xu, W.Y. Ching, *Phys. Rev. B* **44**, 48 (1991). <https://doi.org/10.1103/PhysRevB.44.11048>
40. G.L. Tan, M.F. Lemon, D.J. Jones, R.H. French, *Phys. Rev. B* **72**, 1885 (2005). <https://doi.org/10.1103/PhysRevB.72.205117>
41. D.M. Roessler, W.C. Walker, *Phys. Rev.* **159**, 733 (1967). <https://doi.org/10.1103/PhysRev.159.733>
42. L. Fiermans, R. Hoogewijs, G. Meyer, J. Vennik, *Phys. Status Solidi A* **59**, 569 (1980)
43. B. Nourozi, A. Aminian, N. Fili, Y. Zangeneh, A. Boochani, P. Darabi, *Results Phys.* **12**, 2038 (2019). <https://doi.org/10.1016/j.rinp.2019.02.054>
44. J.P. Perdew, *Int. J. Quantum Chem.* **28**, 497 (1985). <https://doi.org/10.1002/qua.560280846>
45. M. Topsakal, E. Aktürk, S. Ciraci, *Phys. Rev. B* **79**, 115442 (2009). <https://doi.org/10.1103/PhysRevB.79.115442>
46. R. Beiranvand, S. Valedbagi, *Diam. Relat. Mater.* **58**, 190 (2015). <https://doi.org/10.1016/j.diamond.2015.07.008>
47. K. Zollner, M. Gmitra, J. Fabian, *Phys. Rev. B* **99**(12), 125151 (2019). <https://doi.org/10.1103/PhysRevB.99.125151>
48. A. Shrivastava, S. Saini, S. Singh, *Physica B Condens. Matter* **624**, 413390 (2022). <https://doi.org/10.1016/j.physb.2021.413390>
49. G. Cassaboïs, P. Valvin, B. Gil, *Nat. Photonics* **10**, 262 (2016). <https://doi.org/10.1038/nphoton.2015.277>
50. R.J.P. Román, F.J.R.C. Costa, A. Zobellic, C. Elias, P. Valvin, G. Cassaboïs, B. Gil, A. Summerfield, T.S. Cheng, C.J. Mellor, P.H. Beton, S.V. Novikov, L.F. Zagonel, *2D Mater.* **8**, 044001 (2021). <https://doi.org/10.1088/2053-1583/ac0d9c>
51. K.W. Bø Hunvik, P. Loch, D. Wallacher, A. Kirch, L.P. Cavalcanti, M. Rieß, M. Daab, V. Josvanger, S. Grätz, F. Yokaichiya, K.D. Knudsen, C. Rodrigues Miranda, J. Breu, J.O. Fossum, *Langmuir* **37**, 14491 (2021). <https://doi.org/10.1021/acs.langmuir.1c02467>
52. P. Hohenberg, W. Kohn, *Phys. Rev. B* **136**, 864 (1964). <https://doi.org/10.1007/BF01198136>
53. W. Kohn, L.J. Sham, *Phys. Rev.* **140**, 1133 (1965)
54. K. Berland, P. Hyldgaard, *Phys. Rev. B* **89**, 035412 (2014). <https://doi.org/10.1103/PhysRevB.89.035412>
55. J.M. Soler, E. Artacho, J.D. Gale, A. García, J. Junquera, P. Ordejón, D. Sánchez-Portal, *J. Phys. Condens. Matter* **14**, 2745 (2002). <https://doi.org/10.1088/0953-8984/14/11/302> □